Journal of Materials Chemistry A

ROYAL SOCIETY OF CHEMISTRY

PAPER

View Article Online
View Journal | View Issue

Cite this: J. Mater. Chem. A, 2024, 12, 10991

MXene/CdS photothermal–photocatalytic hydrogels for efficient solar water evaporation and synergistic degradation of VOC†

Zhen-Yu Wang,[a] Lei Xu,[a] Cai-Hua Liu,[a] Sheng-Jie Han,[a] Ming-Lai Fu *[a] and Baoling Yuan*[ab]

Solar-driven interfacial water evaporation technology (SIET) is an emerging method for achieving sustainable production of clean water. Most available studies have focused on improving the evaporation efficiency of water, while less attention has been paid to the enrichment of evaporated organic contaminants, especially volatile organic compounds (VOCs) in distilled water, which is one of the key challenges in SIET. Herein, Ti_3C_2 MXene/CdS (MC) nanomaterials were synthesized by acid etching and hydrothermal methods, and MC composite hydrogels (MCHs) with synergistic effects of photothermal evaporation and photocatalysis were successfully prepared by crosslinking foaming polymerization. The water evaporation rate of optimal MCHs was 1.80 kg m^{-2} h^{-1} and the photothermal conversion efficiency of 82.80% could be achieved under one sun irradiation. Most importantly, MCHs significantly degraded a variety of organic contaminants in wastewater, among which the photodegradation rate of a typical VOC (phenol) was 85.12%, and the antibiotic metronidazole was completely removed. This research inferred that the MC hydrogels could be the promising synergistic photothermal evaporation and photocatalytic materials, providing a potential pathway for sustainable clean water production in the SIET field.

Received 3rd January 2024
Accepted 25th March 2024

DOI: 10.1039/d4ta00038b

rsc.li/materials-a

1 Introduction

In the past decades, owing to population growth, climate change, environmental deterioration, and industry expansion, the shortage of freshwater resources has become one of the world crises. To alleviate the problem of water shortage, scientists have developed a variety of water treatment technologies to obtain clean water, including reverse osmosis,[1] electrodialysis,[2] and membrane distillation.[3] However, these technologies suffer from problems such as high energy consumption and secondary pollution. Comparably, solar-driven interfacial water evaporation technology (SIET) has attracted increasing attention in seawater desalination,[4] wastewater purification,[5] and clean water production[6] due to its green, efficient, and low energy consumption virtues. To date, various promising photothermal materials such as organic semiconductors,[6] carbon-based materials,[7,8] polymers,[9] and plasma nanoparticles[10,11] have been developed and tested in SIET. Nevertheless, water evaporation efficiency highly depends on the light absorption rate, heat transfer efficiency and water transport ability.[12,13] Therefore, it remains a challenge to construct the composites for effectively obtaining clean water by use of SIET. On the other hand, many organic contaminants are commonly present in wastewater, including volatile organic compounds (VOCs), which can be easily enriched in condensed water with steam migration during the solar-driven water evaporation process.[14–16] This could seriously affect water quality; however, it has remained a less researched area. Therefore, the effective removal of various organic contaminants, especially VOCs, is an urgent issue to solve in the SIET systems. Recently, photocatalysis coupled with photothermal water evaporation[17,18] has become a viable strategy to remove contaminants and produce drinking water. For instance, Ma *et al.* have prepared a porous sponge incorporated with BiOBrI photocatalyst as a solar evaporator, and the high rejection of VOCs in the evaporated water can be confirmed when river water containing extra added phenol was used as source water.[19] It is well known that as a typical metal sulfide, CdS belongs to one of the efficient semiconductor photocatalysts. It is inexpensive and easy to obtain with relatively narrow bandgap,[20,21] which can effectively degrade various organic contaminants in the aqueous solution. While, MXene, as one of two-dimensional (2D) layered transition metal carbides and nitrides, exhibits tunable band gap and

[a]Xiamen Key Laboratory of Municipal and Industrial Solid Waste Utilization and Pollution Control, College of Civil Engineering, Huaqiao University, Xiamen, Fujian 361021, P. R. China. E-mail: mlfu@iue.ac.cn; mlfu@hqu.edu.cn; yuanbl@hotmail.com; Fax: +86 592 6162705; Tel: +86 592 6162705

[b]Key Laboratory of Songliao Aquatic Environment, Ministry of Education, Jilin Jianzhu University, Changchun, 130118, P. R. China

† Electronic supplementary information (ESI) available. See DOI: https://doi.org/10.1039/d4ta00038b

specific surface area, good hydrophilicity, surface activity, chemical stability, and unique local surface plasmon resonance (LSPR) effect.[22,23] Titanium carbide (Ti_3C_2) is a typical MXene material, which has wide application in environmental remediation,[24] energy catalysis,[25] *etc.*, and has also been suggested as an excellent photothermal conversion material.[26] In addition, Ti_3C_2 MXene has high redox capacity and abundant hydrophilic functional groups (–F, –OH, or –O) on the surface, which allows it to be in close contact with CdS,[20,27] significantly enhancing the photo-induced electron and hole separation rate, reducing charge recombination, and improving photocatalytic activity. In typical examples, Liang *et al.* applied Ti_3C_2/CdS nanorod composites to treat radioactive wastewater.[21] It was found that the photocatalytic reduction efficiency of the composites for uranium(VI) reached 97%, and the composites showed excellent performance under different pH conditions. Chen *et al.* designed 2D/2D CdS nanosheets (NS)@Ti_3C_2 MXene composites for highly photocatalytic hydrogen production.[20] The enhancement of the photocatalytic performance of the composites can be explained by the strong physical and electronic coupling effect between CdS and Ti_3C_2 MXene. However, the performance of the photothermal evaporation and photocatalysis based on the combination of CdS and Ti_3C_2 MXene evaporator in the SIET has not been explored.

Herein, the acrylamide hydrogels consisting of Ti_3C_2 MXene and CdS nanoparticles (MC) were first fabricated and used for efficient evaporation of water and synergistic photocatalytic removal of various organic contaminants. MC hydrogels showed excellent vapor generation capacity and the water evaporation rate was 1.80 kg m^{-2} h^{-1}. Meanwhile, the hydrogel has superior purification performance for metronidazole and a typical VOC (phenol), which are usually enriched in condensed water. This work inferred that MC hydrogels are the promising synergistic photothermal evaporation and photocatalytic materials, providing a potential pathway for sustainable clean water production in the SIET field.

2 Experimental section

2.1 Chemicals and materials

All analytical-grade chemicals involved in the experiments were directly used as received. Titanium aluminum carbide (Ti_3AlC_2) was supplied by Jilin 11 Technology Co., Ltd. Lithium fluoride (LiF), hydrochloric acid (HCl, 36–38 wt%), *N*,*N*-methylenebisacrylamide (MBA), acrylamide (AM), *N*,*N*,*N*′,*N*′-tetramethylethylenediamine (TMEDA), sodium lauryl sulfate (SDS), ammonium persulfate ($(NH_4)_2S_2O_8$) and rhodamine B (RhB 95%), phenol were provided by Sinopharm Corporation and Aladdin. The experimental deionized water (DIW) was prepared using a PSDK ultrapure water machine (Beijing Zihan Century Technology Co., Ltd).

2.2 Methods

2.2.1 Synthesis of Ti_3C_2 MXene. Ti_3C_2 MXene was obtained by selectively etching the Al layer in Ti_3AlC_2 with a mixture of LiF/HCl.[22,28] In a typical synthesis, 2 g of LiF was dissolved in 40 mL of 9 M HCl solution and stirred magnetically for 10 min, and then 2 g of Ti_3AlC_2 powder was slowly added to the above-mixed solution under stirring. It is worthwhile to note that the process needs to be very slow to prevent the solution from boiling and reacting for 24 hours under the condition of a 40 °C water bath. The etched black suspension was centrifuged and the pellet was washed alternately with DIW and absolute ethanol (10 000 rpm for 5 min each) until the pH of the supernatant was 6–7. Finally, Ti_3C_2 powder was dried in an oven at 60 °C for 12 h to obtain the desired MXene.

2.2.2 Synthesis of CdS and Ti_3C_2 MXene/CdS (MC) composites. CdS was prepared according to the reported hydrothermal method.[20,27] First, a certain amount of $CdCl_2 \cdot 2.5H_2O$ was added to DIW (50 mL), sonicated for 5 min, and then magnetically stirred for 1.5 h at room temperature. Then, 0.0042 mol of thiourea and the above-mixed solution were added into a 100 mL of polytetrafluoroethylene autoclave, and heated at 180 °C for 20 h. After natural cooling to room temperature, the pellet was collected by centrifugation, washed several times alternately with DIW and ethanol, and dried at 60 °C for 12 h. According to the different weight ratios of Ti_3C_2 MXene and CdS (2 : 1, 1 : 1, 1 : 2), the obtained Ti_3C_2 MXene/CdS (MC) composites were named MC-1, MC-2, and MC-3.

2.2.3 Synthesis of Ti_3C_2 MXene/CdS hydrogels (MCHs). Firstly, blank hydrogels (BH) were prepared according to the cross-linked foam polymerization method developed by our research group (Fig. 1),[29–32] without adding Ti_3C_2 MXene, CdS, and MC. In a typical preparation, 7.2 g of AM and 0.6 g of MBA were dispersed in 20 mL of DIW using ultrasound, first. Then, under strong mechanical stirring, 0.05 g of SDS was added to foam the mixed slurry for 10 min, which required slow injection of the catalyst of TMEDA to maintain the foamed slurry at a certain volume. Finally, $(NH_4)_2S_2O_8$ was used as the initiator to promote the gelation reaction of the slurry to form a solid hydrogel. The obtained hydrogels were washed off the surface impurities and soaked in DIW for storage, and the water was replaced every 12 h.

MC hydrogels (MCHs) were prepared by assembling MC composites on the BH backbone by multi-dip coating (Fig. 1). The obtained BH was first cut to the desired size and freeze-dried for 24 hours prior to usage. Second, the dried gel was immersed in the MC dispersion (50 mg mL^{-1}) for 10 min and the process was repeated several times to ensure that MC composites were fully impregnated in BH. The resulting hydrogels were labeled MH, MCH-1, MCH-2, MCH-3, and CH, in which the corresponding weight ratios of Ti_3C_2 MXene to CdS were 1 : 0, 2 : 1, 1 : 1, 1 : 2, and 0 : 1, respectively.

2.3 Characterization

The surface morphology, microstructure, and elemental distribution of samples were observed using the Zeiss Sigma 300 scanning electron microscope (SEM), energy dispersive spectrometer (EDS), and FEI Tecnai G2 F20 S–Twin transmission electron microscope (TEM), respectively. The crystal structure of the samples was analyzed by X-ray diffractometer (XRD). UV-visible-near-infrared (NIR) diffuse reflectance spectra of the

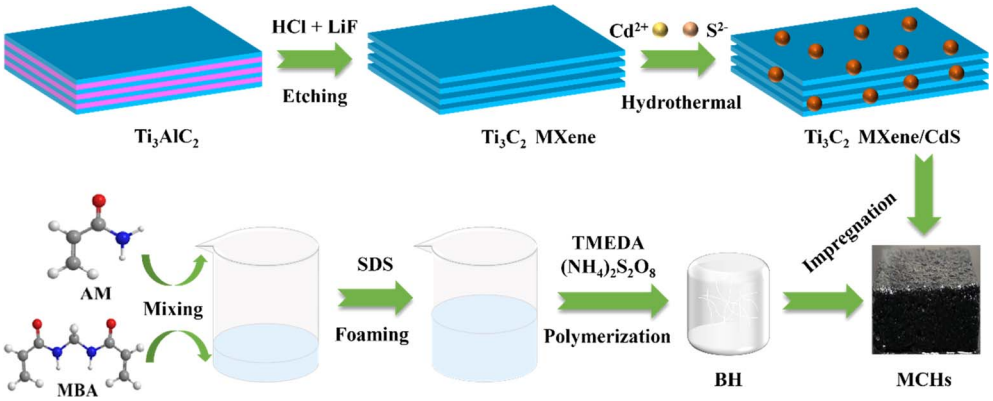

Fig. 1 Preparation of Ti_3C_2 MXene/CdS hydrogels.

samples were measured using a UV-3600 spectrophotometer from Shimadzu, Japan. The elemental composition and chemical functional groups of the samples were evaluated using Bruker TENSOR27 Fourier transform infrared absorption spectroscopy (FTIR) and the Thermo Fisher Scientific K-Alpha X-ray photoelectron (XPS) spectrometers. Raman spectroscopy was performed with the help of the Horiba JobinYvon LabRAM HR Evolution, France, instrument. The DSA100 contact angle measuring instrument, Germany, was used to evaluate the surface hydrophilicity of the hydrogels. A JES-FA300 electron spin resonance spectrometer (ESR), Japan, was used to identify the species of the reactive radicals.

2.4 Interfacial water evaporation experiment

The interface water evaporation experiment (experimental environmental conditions: humidity 30 ± 1%, temperature 24 ± 0.5 °C) under a solar simulator (PLS-SXE300+, Perfectlight) using a standard AM 1.5G optical filter with a light flux range of 0.5 to 3.0 kW m^{-2}. The irradiation intensity of the MCHs' surface was determined using an optical power meter (CEL-NP2000-2, Aulight). Specific MCHs were used as evaporators and polystyrene (PS) foam was used to support them on a vacuum-insulated glass beaker with an inner diameter of 4.5 cm, and the beaker was filled with a certain volume of water, PS foam completely covered the water surface for heat insulation and also avoided escape of water from the gap between the glass and the foam during evaporation, and the commercial skim cotton strip vertically through the PS foam was used as a water delivery medium to connect the MCHs at the top with the water at the bottom. The water weight change was recorded every 1 minute using an electronic balance (Ohaus, PX224ZH/E, accuracy 0.0001 g) connected to a computer. The surface temperature change of MCHs under light conditions was measured using a thermal infrared imager (FLIR, ONE Pro AND). Schematic and a digital photo of a solar-driven interfacial water evaporation device are shown in Fig. S1.†

Calculation of the solar-vapor conversion efficiency of hydrogels:

$$\eta = m \times h_{LV}/(C_{opt} \times P_0) \quad (1)$$

where m is the evaporation rate of water (considering the effect of natural evaporation, kg m^{-2} h^{-1}), h_{LV} is the equivalent evaporation enthalpy of water in the hydrogels (J g^{-1}), C_{opt} is the surface optical concentration of the photothermal evaporation materials, and P_0 is the non-limit solar radiation value.

2.5 Evaluation of photocatalytic performance

The photocatalytic performance of the MC composites was evaluated by RhB simulating the degradation of wastewater. In this experiment, a Xenon lamp (PLS-SXE300+, Perfectlight) was used as the visible light source (λ > 420 nm), and the light intensity at the double-jacketed beaker liquid level was set to 1.0 kW m^{-2}, and the temperature of the solution was maintained at room temperature through the continuous flow of circulating water. The photocatalysts (12 mg) were added to RhB (10 mg L^{-1}, 40 mL) solution and placed in a dark environment with magnetic stirring for 30 minutes to achieve adsorption equilibrium, followed by the light turned on, and samples (2 mL) were taken every 20 minutes to detect the remaining concentration of RhB.

The degradation rate (DR) of RhB is calculated as follows:

$$DR = C_t/C_0 \quad (2)$$

where C_t is the concentration of RhB solution at different time points, and C_0 is the initial concentration of RhB solution.

2.6 *In situ* photodegradation of organic contaminants

The *in situ* photocatalytic removal of organic contaminants during photothermal evaporation was carried out using a laboratory-made device (Fig. S2†), in which phenol was used as a model VOC contaminant. The evaporator in the device was the same as that described in Section 2.4 except that a phenol solution (10 mg L^{-1}) was used instead of pure water, a condensate collection device was built using a Petri dish and an inverted beaker, and the connection between the two was tightly attached with parafilm to ensure the tightness of the device. The phenol concentration in the condensate was detected at λ = 270 nm using a dual-beam UV/vis spectrophotometer (TU-1901, general analysis). In addition, to evaluate the possible

application of MCHs, the antibiotic metronidazole (MNZ) was also selected as a target organic contaminant in the experiment to study the removal efficiency of regular contaminants in wastewater under the same experimental conditions.

3 Results and discussion

3.1 Characterization

Under the combined reaction of LiF and HCl (Fig. 1), the accordion-like multilayer MXene can be obtained by selectively etching the Al layer in Ti_3AlC_2. Compared with the dense blocky structure of Ti_3AlC_2, the layered structure of Ti_3C_2 MXene was clear and loosely stacked, forming an open interlayer nanoscale gap (Fig. 2a and b), which is similar to the structural change described previously.[33,34] The morphology and microstructure of Ti_3C_2 MXene were further analyzed by TEM and HRTEM. As can be observed from Fig. S3c,† MXene shows a nanosheet-like structure, with dark areas mainly formed by the orderly stacking of multiple nanosheets. In addition, a lattice fringe with a plane spacing of 0.155 nm can also be indexed, as shown in Fig. S3d,† which belongs to the (100) plane of MXene. The crystal structure characteristics of Ti_3C_2 MXene, CdS, and MC composites were further analyzed by XRD. As shown in Fig. 2c, the typical (104) crystal plane corresponding to the diffraction peak signals ($2\theta = 39.0°$) in the Ti_3AlC_2 diffraction pattern (JCPDS #2-0875), as well as the characteristic peak signals of 34.0° and 41.8°, disappeared significantly in the Ti_3C_2 spectrum. The reason can be ascribed to that the Ti–Al weak metal bond in Ti_3AlC_2 was broken by the acid etching and the Al element was removed, in which Ti_3AlC_2 was successfully converted to Ti_3C_2.[35,36] Compared with the diffraction peaks of Ti_3AlC_2, those of pure Ti_3C_2 are shifted to smaller angles, in which the characteristic diffraction peaks shift from 9.5° and 19.1° to 8.9° and 18.0°, corresponding to (002) and (004) crystal planes, respectively. In addition, the diffraction peaks of Ti_3C_2 appeared more widen (Fig. S3a†), which means that the layer spacing of MXene nanosheets was expanded and multilayer structures were formed.[36,37] The inferred results are in

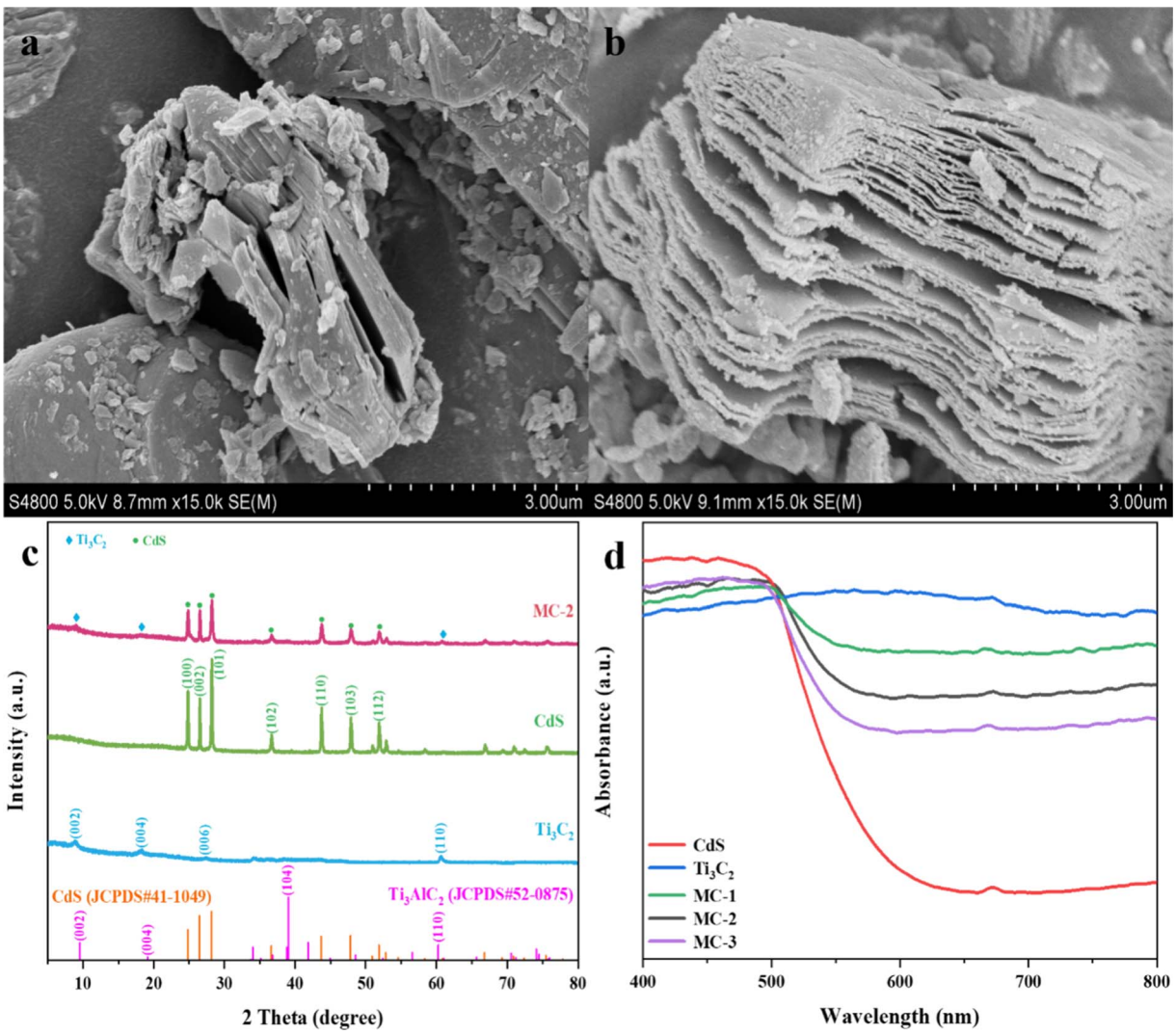

Fig. 2 SEM images of (a) Ti_3AlC_2 and (b) Ti_3C_2 MXene. (c) XRD spectra of Ti_3C_2 and MC-2. (d) DRS spectra of Ti_3C_2, CdS, and MC composites.

accordance with the observations from the SEM images. The diffraction peaks at 27.3° and 60.5° are related to the crystal planes of (006) and (110),[20,27] respectively, indicating that the as-prepared Ti_3C_2 has good crystallinity. While, some diffraction peaks can be hardly observed, which may be the presence of some MAX phase impurities. Similar phenomena have also been indicated in the previous studies.[36]

For CdS, the diffraction peaks at 24.8°, 26.5°, 28.2°, 36.6°, 43.7°, 47.9°, and 51.8° closely match the crystal planes (100), (002), (101), (102), (110), (103), and (112) of the standard spectrum (JCPDS #41-1049)[21,27] (Fig. 2c and S3b†), respectively. For the diffraction pattern of MC composites, both characteristic peaks of Ti_3C_2 and CdS appeared. As indicated in Fig. S3b,† with the increase of CdS content, the diffraction intensity of CdS increased, but the position of the peaks did not change significantly, indicating that CdS and Ti_3C_2 were effectively coupled and did not affect the crystal structure.[21,27,36] It is worthwhile to mention that the above results may indicate that the photocatalytic activity (see below) of MC composites is mainly related to the catalytic effect of CdS in the samples, rather than the crystal structure change of Ti_3C_2.

The optical absorption properties of Ti_3C_2 MXene, CdS, and MC composites were measured by UV-vis-NIR DRS spectroscopy. As shown in Fig. 2d, CdS exhibits good absorption in visible light, while Ti_3C_2 MXene, due to its inherent metallic properties, exhibits a full range of light absorption without obvious absorption band edges.[20,36] As a result, the light absorption of MC composites is not as good as that of Ti_3C_2 MXene, but with the decreased ratio of yellow CdS to black Ti_3C_2 MXene in the composites, the absorption edge of the composites is redshifted, and the light absorption at 500 ~ 800 nm is enhanced. It can be explained that the LSPR effect of Ti_3C_2 accelerates the oscillation and transition of the excited thermal electrons under sunlight irradiation, and more energy is generated by photothermal conversion[26,38] which can be indicated in the following photothermal evaporation performance study. However, too much Ti_3C_2 could easily obscure the catalytic effect of CdS,[20,21,39,40] which agrees with the fact that CdS in the samples is responsible for the photocatalytic activity of MC composites.

SEM images in Fig. 3 show the microscopic morphology of the hydrogels, and it can be seen clearly that the hydrogels present a 3D porous structure, which could provide abundant water transport channels.[41] The specific porous structure of hydrogels could also extend the refractive path of the incident light, which is conducive to the aggregation and absorption of light and creates good conditions for evaporation.[30,31] Moreover, the high surface areas of the porous structure enhance the inclusion of organic contaminants in the hydrogels, which usually is required for the improved photocatalytic performance of the MC composite hydrogels. Compared with the smooth surface of the blank hydrogel (Fig. 3a), the embedding of the MC agent further increases the surface areas of the composite hydrogels, which is indicated by the rough surface of MC hydrogels (Fig. 3 and S4†). It is worthwhile to mention that the introduction of MC nanomaterials does not affect the 3D porous backbone of the hydrogels (Fig. 3d–f and S4†). The inclusion of multiple layers of MXene in the gel can be observed clearly from the surface, implying the successful incorporation of MXene photothermal materials. The uniform distribution of CdS nanoparticles as well as MXene can be seen in the surface of hydrogel also indicating the successful incorporation of CdS photocatalysts from MCHs. The chemical compositions of MCHs were further characterized by EDS element mapping spectra, and it can be seen from Fig. 3g that the Ti, Cd, S, O, and C elements are homogeneously distributed in the MCHs, which indicates the successful incorporation of the MC composites into the hydrogels backbone.

In addition, FTIR, Raman, and XPS spectroscopy were used to study the interactions and chemical compositions of MC hydrogels. As shown in Fig. 4a, for FTIR, the main band signals in the spectrum are related to the characteristic absorption peaks of polyacrylamide (PAM). Specifically, the wide band of 3175–3447 cm^{-1} is mainly attributed to the strong vibration of the O–H group (water molecules absorbed by amides) and the –NH_2 group. The strong vibration assigned to the C=O group by the absorption peak can be observed at 1637 cm^{-1}. The characteristic peak at 1401 cm^{-1} exhibits C–N bond stretching.[29–32] These abundant functional groups assure hydrogels with good hydrophilicity, which might form many hydrogen bonds between the PAM hydrogel and MC, promoting the transportation of water in the MC hydrogels. Raman spectra of MXene, CdS, and MC composites are shown in Fig. 4b, and the peaks at 411 cm^{-1} and 627 cm^{-1} correspond to the E_g group vibrations of Ti, C, and surface functional group atoms.[28,42,43] The Raman peak of the MC-2 composite is observed to shift towards a lower wavenumber, indicating the interaction between MXene and CdS in MC-2.[44]

XPS analysis of MCHs is shown in Fig. 4c, and only O 1s, C 1s, and N 1s characteristic peaks can be detected in the BH sample. For the MXene hydrogel, Ti 2p as well as additional weak F 1s characteristic peak can be observed due to the introduction of Ti_3C_2. For the MCH samples, due to the incorporation of CdS nanoparticles in the hydrogels, Cd 3d and S 1s characteristic peaks can also be detected in MCHs. While, compared to BH, the peak intensity of the C, O, and N elements of MH and MCHs varied, which may be explained by the way that the addition of MXene and MC masks the surface groups of BH, weakening its signal intensity, or forming new chemical bonds, which reduce the signal intensity of the BH surface groups.[45] To further gain insight into the interaction between Ti_3C_2 MXene and CdS, high-resolution XPS spectra analyses were conducted on the chemical element compositions and corresponding bond states in MC composites (Fig. S5†). Fig. S5a† shows the high-resolution XPS spectrum of Ti 2p, and the binding energies of 455.48 and 460.58 eV are deconvoluted into Ti $2p_{3/2}$ and Ti $2p_{1/2}$ double states, which are related to the formation of Ti–C bonds in composites.[21,36] The three peaks in the Ti 2p spectrum at 456.63, 458.33, and 463.49 eV are attributed to Ti_xO_y $2p_{3/2}$, Ti–O $2p_{3/2}$, and Ti–O $2p_{1/2}$, respectively, due to the abundant oxygen-containing functional groups attached to the catalyst surface or possibly slight oxidation of Ti_3C_2.[21,27,36,39] The fitting peak corresponding to Ti $2p_{3/2}$ at 455.48 eV is concerned with F ions adsorbed on the surface of Ti_3C_2.[36] Five distinct characteristic peaks (284.04, 284.78, 285.69, 286.36, and 287.82 eV) were

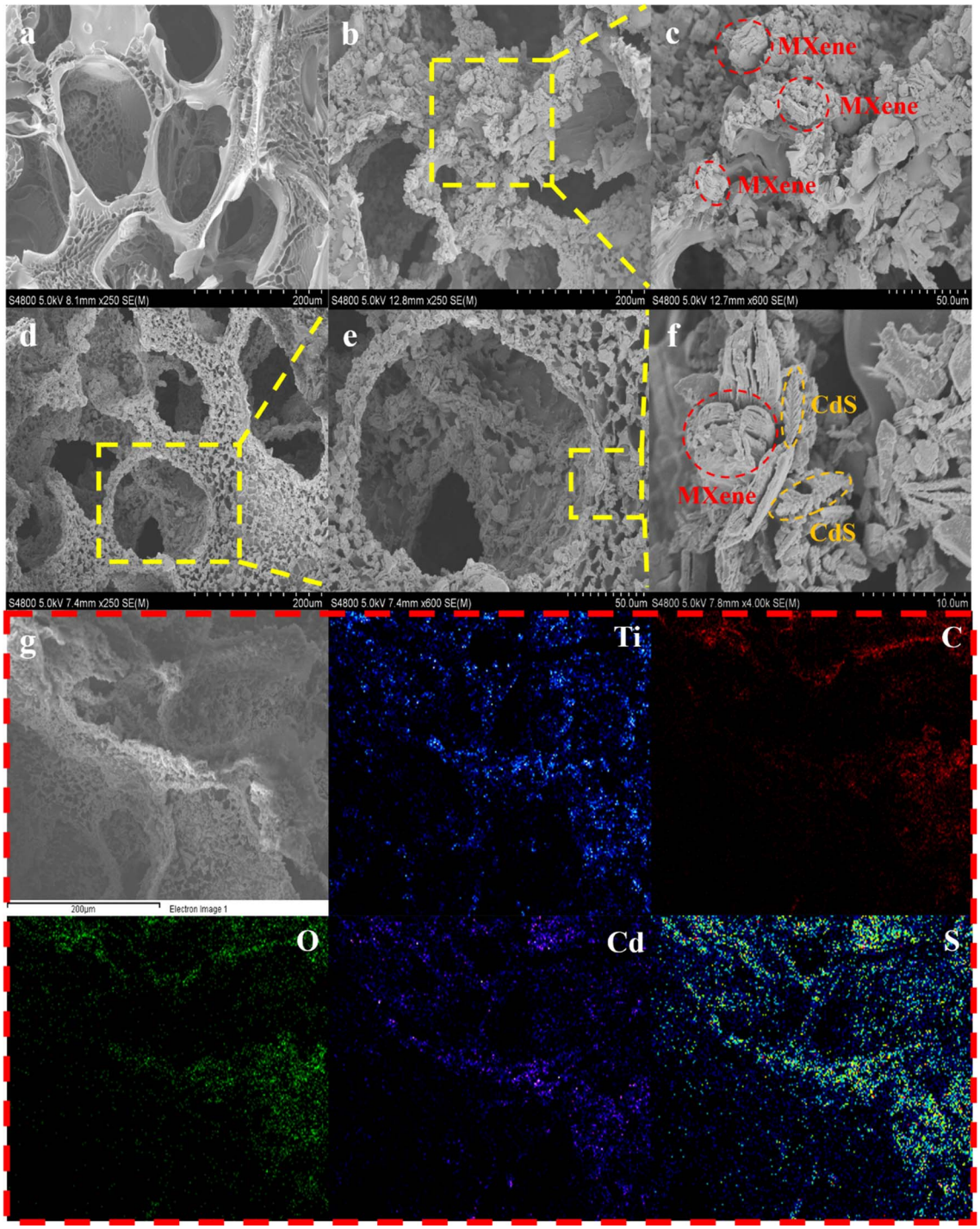

Fig. 3 SEM images of (a) BH, (b and c) MH, and (d–f) MCH-2. (g) EDS elemental mapping diagrams corresponding to Ti, C, O, Cd, and S in MCH-2.

observed in the C1s spectrum (Fig. S5b†), representing C–Ti, C–C, C–O–C, C–O, C–O, and C–F bonds, respectively, which also reflected the existence of –O and –F terminal groups.[27,40,46] Among them, the formation of C–O–C bonds is attributed to the slight oxidation of the materials in a hydrothermal reaction.[36] From the above Ti 2p and C 1s high-resolution XPS spectroscopy, it can be seen that the MC composites can provide effective active sites for the removal of organic contaminants.[39] The XPS spectra of Cd 3d are shown in Fig. S5c,† and the double typical spin–orbit diffraction peaks at 405.03 and 411.68 eV are ascribed to Cd $3d_{3/2}$ and Cd $3d_{5/2}$, respectively, which match greatly with Cd^{2+} in CdS.[39,46] The double characteristic peaks of the S 2p spectrum at 161.38 and 162.63 eV binding energies are related to S $2p_{3/2}$ and S $2p_{1/2}$ of S^{2-} in CdS (Fig. S5d†).[20] The above results fully illustrate the successful combination of Ti_3C_2 MXene and CdS.

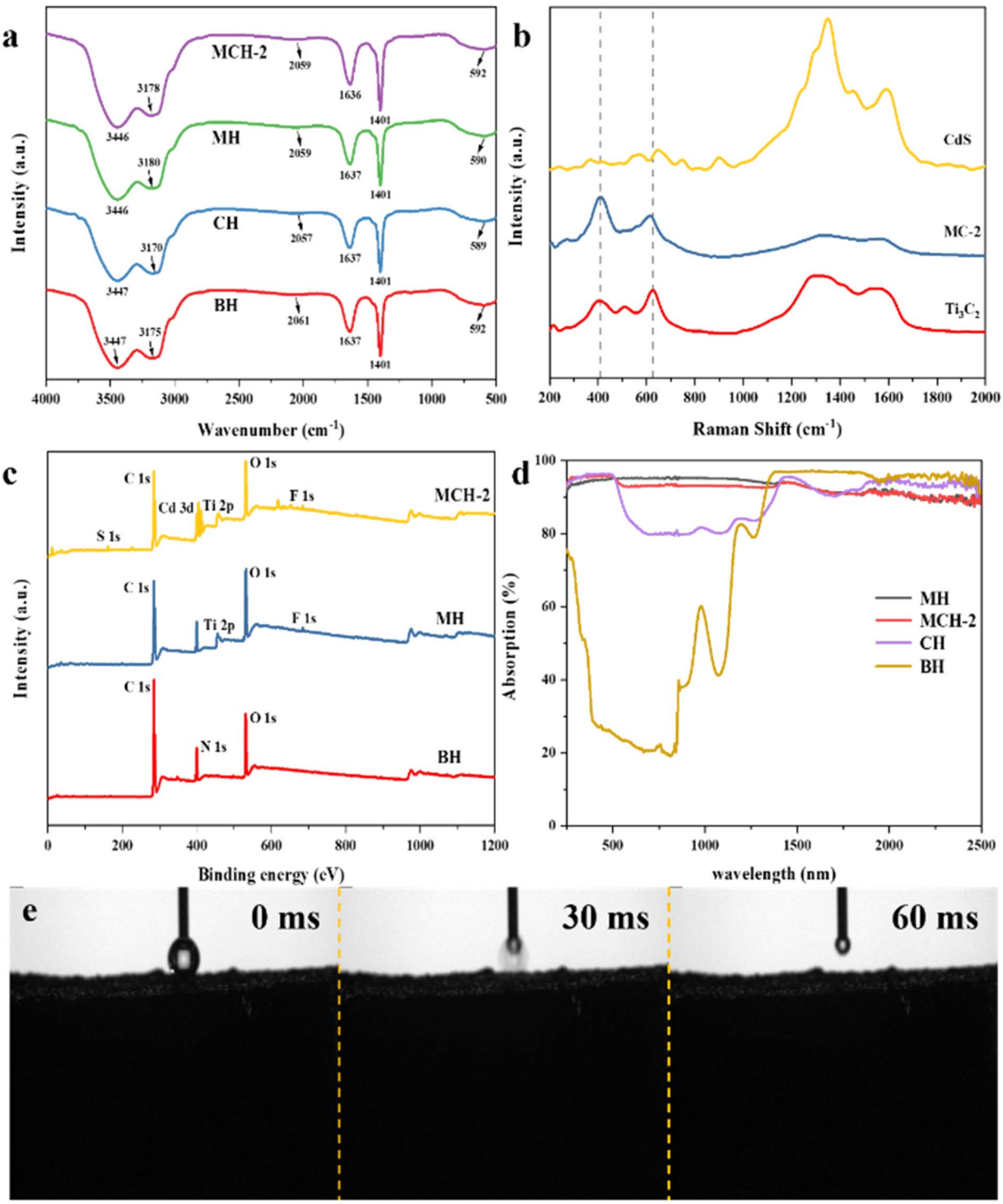

Fig. 4 (a) FTIR spectra of BH, CH, MH, and MCH-2. (b) Raman spectroscopy of Ti_3C_2, MC-2, and CdS. (c) XPS spectra of BH, MH, and MCH-2. (d) UV/vis-NIR absorption spectra of hydrogels. (e) Surface contact angle of MCH-2.

The optical absorption performance of the serial hydrogels was measured using UV/vis-NIR spectroscopy. It can be seen from Fig. 4d and S6† that compared with BH, the light absorption rates of MCHs are significantly enhanced, and the light absorption rates of MH, MCH-1, MCH-2, and MCH-3 are about 95.3%, 95.1%, 93.1%, and 88.2%, respectively. In addition, the hydrophilicity of hydrogels was studied using a contact angle measuring instrument to confirm their potential application in interfacial water evaporation. As shown in Fig. 4e and S7,† the high-speed camera recorded that the spherical water droplets can quickly diffuse to the hydrogels surface and be fully absorbed between 30 ~ 60 milliseconds (ms). Fig. S8†

shows the distribution of water absorbed by MCHs indicated on the cellulose paper,[47] which can be transported from the lower interface of the MCHs to the upper interface in less than 5 s, and then rapidly spread around the cellulose paper. Based on the time it takes for water to arrive at the surface of the materials, its transport speed is approximately 2.2 mm s^{-1}, which is superior to the data in the literature, such as on attapulgite-based aligned aerogels (0.083 mm s^{-1}),[48] carbon fiber-cotton-based evaporator (0.78 mm s^{-1}).[8] These results indicate that MCHs have excellent water transport ability, which means that water and contaminants in the original solution can quickly migrate to the evaporation interface and catalytic activity area during evaporation, enhancing the solar-driven water production performance and photocatalytic oxidation capacity of MCHs.[49,50]

3.2 Interfacial water evaporation properties of MCHs

The solar-driven interface water evaporation performance of hydrogels was evaluated by recording water loss mass under 1.0 solar irradiation in real time. As shown in Fig. 5b, pure water exhibited the lowest evaporation rate (0.77 kg m^{-2} h^{-1}). However, under the same experimental conditions, the presence of hydrogels significantly increased the mass loss of water. Moreover, the water evaporation amounts of CH, MCH-1, MCH-2, MCH-3, and MH were 4.12, 5.74, 5.39, 4.98, and 6.65 kg m^{-2} in 180 min (Fig. 5a) and the corresponding evaporation rates were 1.37, 1.91, 1.80, 1.66 and 2.21 kg m^{-2} h^{-1}, respectively. Therefore, the solar evaporation efficiencies of different MCHs reached 72.09%, 86.77%, 82.80%, 80.44%, and 98.27%, respectively (Fig. 5b). The as-prepared hydrogels exhibited a superior water evaporation rate than those related to other MXene-based photothermal evaporation materials reported in recent literature (Table S1†). In addition, as shown in Fig. 5c and d, it was found that the amount of water loss increases with the increase of light intensity, and the corresponding evaporation rate also increases. At 2.5 sun irradiation, the evaporation rate of MCH-2 is 3.629 kg m^{-2} h^{-1}, while the photothermal efficiency gradually decreases. This is largely due to the fact that an increase in light intensity will aggravate the heat loss of the evaporation system, thereby affecting the photothermal efficiency.[45]

The surface temperature of photothermal MCHs was monitored using an infrared thermal imaging system. As shown in Fig. 5e, the surface temperature of MCHs increases significantly in a short time, and finally reaches a relatively stable value, in which the equilibrium temperature of MCH-2 is about 34.3 °C,

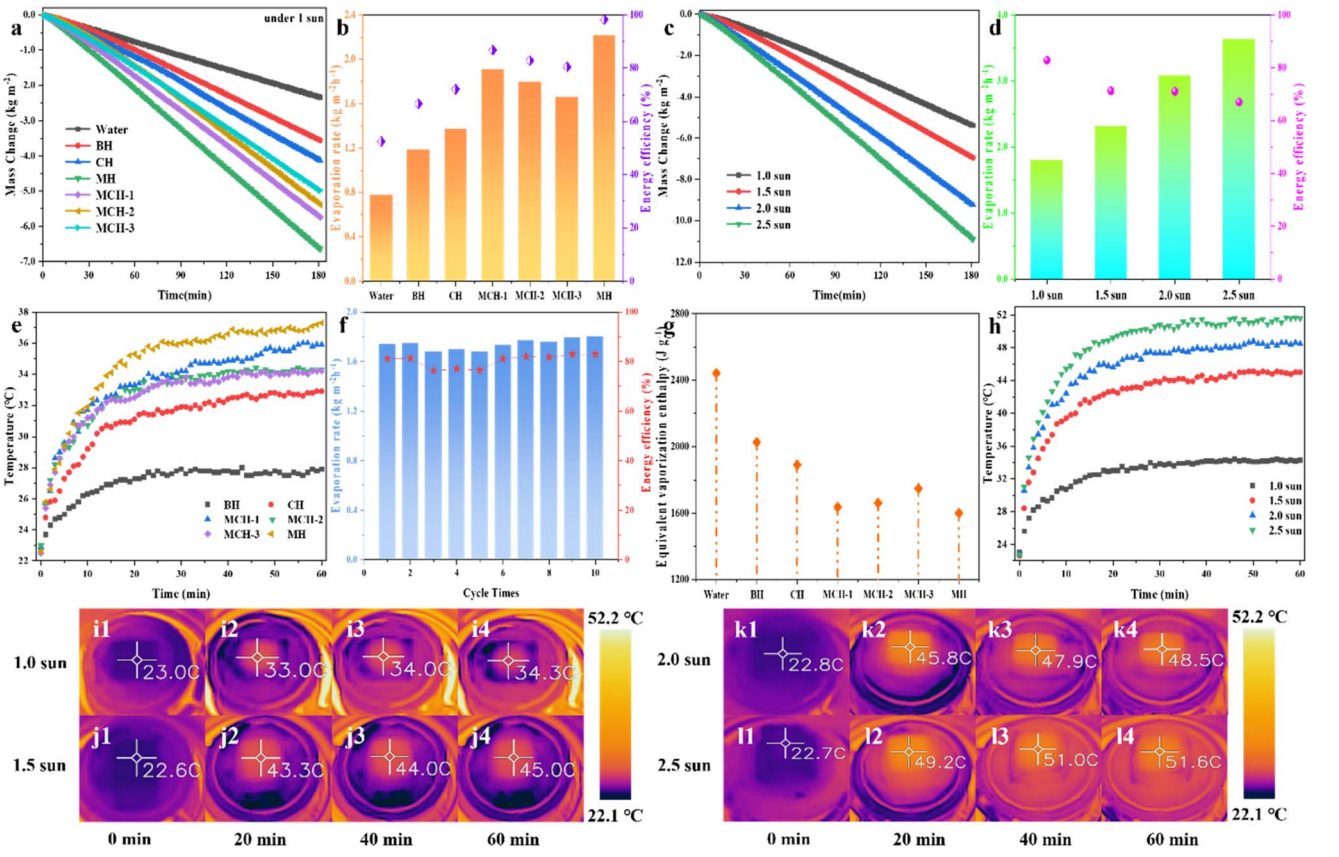

Fig. 5 (a) Mass changes of water over 180 minutes under 1.0 sun irradiation. (b) Evaporation rate and efficiency of different systems under 1.0 sun irradiation. (c) Mass loss of water and MCH-2 under 1.0–2.5 sun exposure. (d) Evaporation rate and efficiency of MCH-2 at 1.0–2.5 solar exposure. (e) Surface temperature of BH, CH, MH, and MCHs within 60 minutes under 1.0 sun irradiation. (f) Water evaporation cycle test of MCH-2 under 1.0 sun irradiation. (g) Equivalent evaporation enthalpy of water in BH, CH, MH, MCHs, and pure water. (h–l) Surface temperature and infrared images of MCH-2 at different time points under different sunlight.

and the increase is 11.3 °C within 60 min. In contrast, BH's surface temperature rises only 5.3 °C in a limited manner. The infrared images of the hydrogels corresponding to different time points are shown in Fig. S9.† This shows that MCHs are promising photothermal materials, that could effectively convert solar energy into heat and concentrate it on the hydrogels surface for effective evaporation. In addition, with the increase in sunlight intensity, the photothermal effect of the hydrogels is more significant. To specify, when the light intensity increased from 1.0 to 2.5 sun, the surface temperature of MCH-2 increased from 34.3 °C to 51.6 °C (Fig. 5h–l). Furthermore, the recyclability of MCH-2 was evaluated by 10 consecutive evaporations. As shown in Fig. 5f, the water evaporation rate and photothermal efficiency of MCH-2 are maintained at a good level, indicating that MCH-2 has stable water evaporation performance and cycling durability. The above results also mean that MXene material exhibits good chemical stability under prolonged cycling experiments, and has little effect on the photothermal conversion efficiency. By calculating the equivalent evaporation enthalpy of water in a hydrogels (Fig. 5g), the relevant calculation formulae and values are shown in S1 and Table S2 of the ESI.† It can be shown that the calculated enthalpy of the MC hydrogels is much lower than that of pure water and blank hydrogel. The reason can be that the abundance of oxygen-containing groups in polymeric hydrogel networks could weaken the interaction of hydrogen bonds between many bounded water clusters in the water molecules. Therefore, during the evaporation process, water molecules are easily driven by the least external energy to release the constraints of these steady-state water clusters and escape from the hydrogel skeleton into the gas.[42,51,52] Under the same energy consumption conditions, MC hydrogels can evaporate more water, which is highly consistent with the solar evaporation efficiency of the hydrogels.

3.3 Photocatalytic property of MC composites

Considering that wastewater contains several organic contaminants that are potentially harmful to human health and the ecological environment, it is difficult to meet the actual demand if only solar evaporation is carried out. Therefore, the introduction of a photocatalytic effect in the process of photothermal evaporation can significantly enhance the practicality of wastewater purification. Herein, the photocatalytic activity of MC composites was further evaluated by using the RhB organic dye as a target contaminant. The removal of organic contaminants by nanoparticle catalysts can be attributed to the adsorption and catalytic degradation processes. Firstly, the static adsorption of RhB by MC composites under dark condition was explored. As can be seen from Fig. 6a, the first 30 min was the rapid adsorption stage of RhB by MC composites, after which the adsorption remained relatively stable. The adsorption rate of RhB by MC-1 was the best among the composite samples, reaching 26.8%. The reason is that the content of Ti_3C_2 with the layered structure in MC-1 is higher, which provides more adsorption active sites for the dye molecules. On

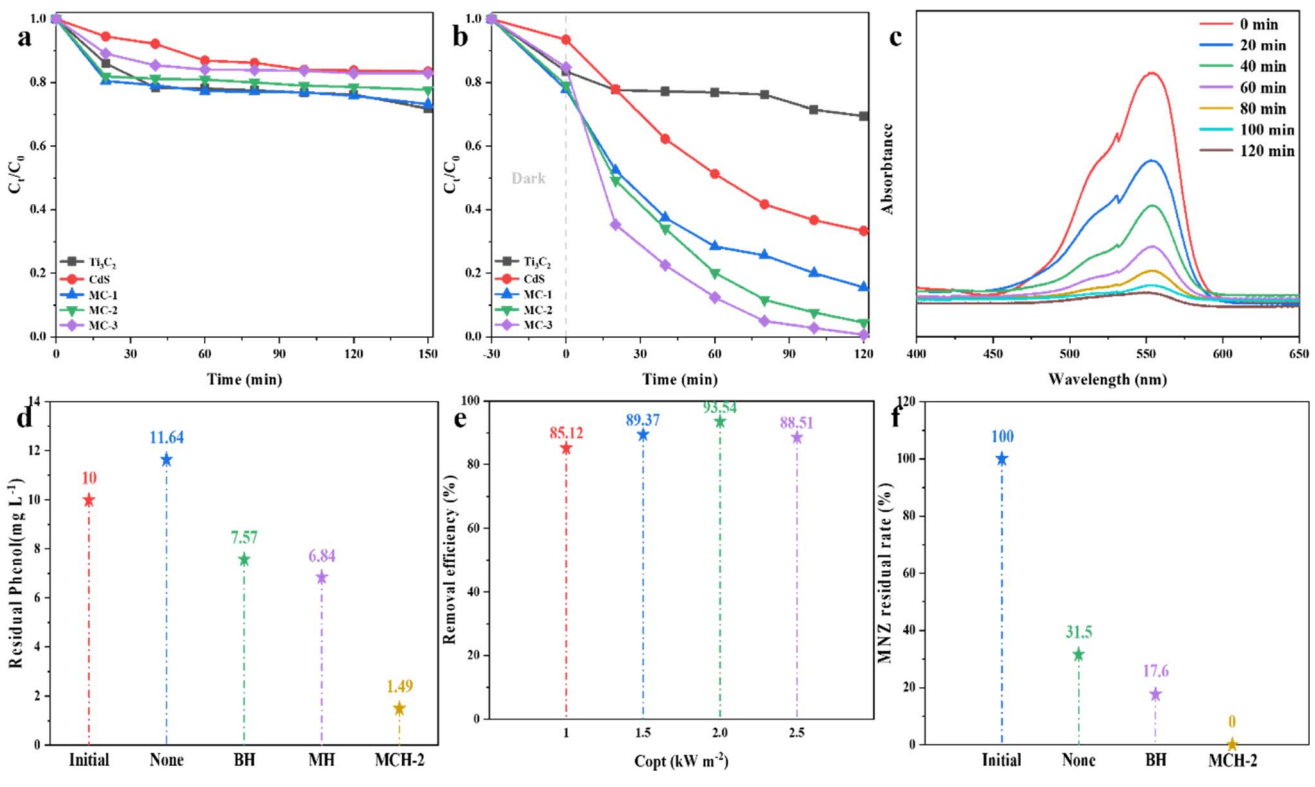

Fig. 6 (a) Static adsorption test of Ti_3C_2 MXene/CdS catalysts. (b) Photocatalytic degradation of RhB by Ti_3C_2 MXene/CdS samples. (c) UV-vis curves of RhB at different reaction times. (d) Removal of phenol by different hydrogels. (e) Removal rate of phenol by MCH-2 at different light intensities. (f) Purification effect of different hydrogels on metronidazole.

the other hand, RhB is a cationic dye, and a large amount of –OH on the surface of MXene can form a strong chemical bond with it, which enhances the adsorption of RhB.[53,54] Fig. 6b shows the photocatalytic activity of different samples for RhB degradation under the simulated sunlight irradiation. The results show that Ti_3C_2 only has slight photocatalytic activity under visible light, which is consistent with previous research results.[55] The photodegradation performance of all the MC composites was better than that of CdS or Ti_3C_2, which means that the combination of CdS and MXene can significantly improve the removal efficiency of RhB. When the ratio of Ti_3C_2 to CdS changed from 2 : 1 to 1 : 1, the degradation rate of RhB increased and exceeded 95% after 120 min of irradiation. Moreover, when the ratio of Ti_3C_2 to CdS further changed to 1 : 2, the catalytic property of MC composites to RhB enhanced further. This result can be attributed to the improved photocatalytic degradation of CdS with higher content. The UV-vis absorption spectra of organic dyes at different irradiation times are shown in Fig. 6c. It can be seen that with the increase of the reaction time, the peak at the characteristic wavelength of RhB is significantly weakened and eventually tends to vanish, indicating that RhB can be effectively removed by the MC catalysts under simulated sunlight.

3.4 Efficient VOCs and organic contaminants purification

With the increase of interface temperature, volatile and semi-volatile organic pollutants (such as phenol) in wastewater are easily enriched into condensed water during the photothermal evaporation process,[56] thereby affecting water quality. Therefore, phenol as a typical VOC was selected as a simulated contaminant to evaluate the *in situ* photocatalytic degradation efficiency of MCHs on VOCs during photothermal evaporation using a laboratory-made evaporation device. The results of Fig. 6d show that the initial concentration of phenol in the solution was 10 mg L^{-1}, and in the blank control experiment without the photothermal evaporation materials, the phenol concentration of 11.64 mg L^{-1} in the evaporated water was higher than the initial concentration, which means that VOCs are easy to escape with steam and be enriched in the condensate, which affects the water quality safety.[19] When BH and MH were present, phenol was only partly removed from the evaporated water at 7.57 mg L^{-1} and 6.84 mg L^{-1}, respectively. However, when the MCH-2 was used, the phenol concentration in the evaporated water was significantly reduced with 1.49 mg L^{-1}. Compared with the MH without the incorporation of a CdS photocatalyst, the removal rate of a VOC was significantly enhanced by MCH-2. It can be explained by the following reasons: (1) the combination of Ti_3C_2 MXene and CdS enhances the light absorption performance of the composites; (2) hydrogels provide a rich porous network structure and surface functional groups, which promote the transport of pollutants and make them fully in contact with the active sites of the photocatalysts, and are degraded by the reactive oxygen species (ROS) generated by photocatalysis[57] under light irradiation; (3) the local photothermal effect generated by the LSPR effect of Ti_3C_2 MXene improves the photocatalytic reactivity.[58] Interestingly, when the light intensity increased to 2.0 sun, the photocatalytic degradation effect of MCH-2 on phenol was the best, and then slightly reduced, but the degradation rate of 88.51% was still maintained at 2.5 sun (Fig. 6e). It may be that when the light intensity is enhanced, the interface evaporation rate is accelerated, and the contact time with the photocatalyst during the upward escape of phenol with steam is insufficient.[19,57,59] The same method was used to study the removal ability of the MC complex hydrogels on antibiotic (MNZ) wastewater during photothermal evaporation. From Fig. 6f, it can be concluded that MCH-2 has a 100% purification effect on MNZ. This shows that MC composite hydrogels can efficiently purify organic contaminants in wastewater and produce clean water with the help of solar-driven mass transfer and photocatalytic performance.

3.5 Synergistic mechanism of MCHs photothermal evaporation/photocatalytic

To study the mechanism of the MC composite photocatalysts more comprehensively, the active radicals generated by MC under light irradiation were identified by electron spin resonance (ESR) technology (Fig. 7). From previous studies, it can be seen that the spin trapper 2,2,6,6-tetramethyl-1-piperidine group (TEMPO) itself has paramagnetism, which can show a strong ESR signal. When photogenerated electrons (e^-) and holes (h^+) are generated on the surface of the catalyst, the two will combine with the single electron of TEMPO, causing TEMPO to lose signal, resulting in a decrease in the signal intensity, to confirm that the electrons and holes are generated in the reaction system.[40,60] It can be concluded that MC-2 exhibits strong ESR signals of TEMPO-e^- under darkness, while the characteristic signal peaks of MC-2 are significantly weakened after illumination, and finally no visible signals are found (Fig. 7a). Compared to MC-2, the signals of CdS are more pronounced under illumination. This indicates that the introduction of Ti_3C_2 MXene has accelerated the generation of more charge carriers bound to TEMPO in MC-2. In addition, superoxide radicals ($^{\bullet}O_2^-$) and hydroxyl radicals ($^{\bullet}OH$) were further identified by 5,5-dimethyl-1-pyrroline-*N*-oxide (DMPO).[40,60] As shown in Fig. 7c and d, no obvious ESR signals of DMPO-$^{\bullet}OH$ and DMPO-$^{\bullet}O_2^-$ additive appeared in the dark environment, indicating that MC and CdS do not generate $^{\bullet}OH$ and $^{\bullet}O_2^-$. After being irradiated by light, the four typical characteristic peaks of DMPO-$^{\bullet}OH$ and DMPO-$^{\bullet}O_2^-$ can be observed. The results indicate that more abundant $^{\bullet}OH$ and $^{\bullet}O_2^-$ are generated in the MC/photocatalytic degradation system. Therefore, the active radical capture test confirmed that e^-, h^+, $^{\bullet}OH$, and $^{\bullet}O_2^-$ play an important photocatalytic oxidation role in the efficient degradation of organic pollutants by MC composites.

Based on the above results, a possible action mechanism for the photocatalytic removal of organic pollutants by MC complex hydrogels during interfacial water evaporation is proposed (Fig. 8). CdS has a suitable band gap to absorb sunlight and produce photocarriers, leaving holes (h^+) in the valence band (VB) when photogenerated electrons (e^-) transit to the conduction band (CB). The coupling of Ti_3C_2 MXene and CdS

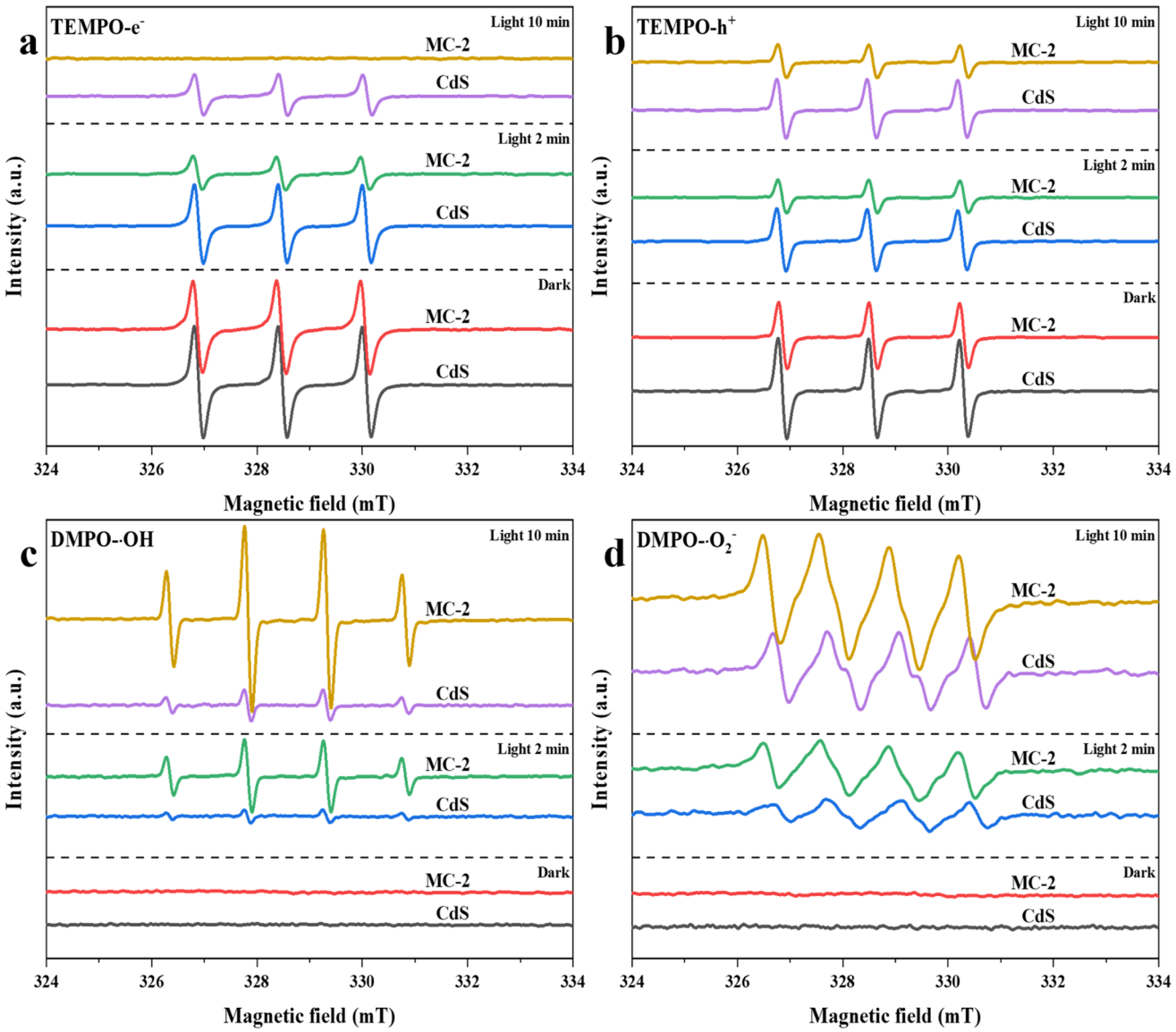

Fig. 7 ESR spectra of (a) TEMPO-e^-, (b) TEMPO-h^+, (c) DMPO-$^{\bullet}OH$, and (d) DMPO-$^{\bullet}O_2^-$ adducts.

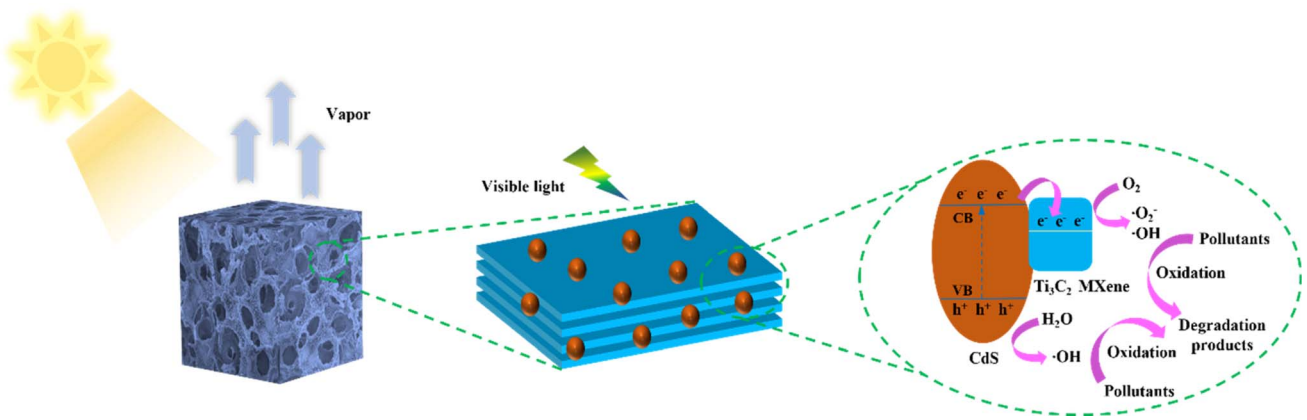

Fig. 8 Schematic diagram of photocatalytic degradation mechanism of Ti_3C_2 MXene/CdS composite hydrogels.

may form a tight interface between the two, through which photogenerated electrons can easily quickly hop to Ti_3C_2 MXene (eqn (3)).[21,40,61] Therefore, Ti_3C_2 MXene can act as a charge transfer medium and electron capture site, accelerating the separation of electrons and holes and extending the lifetime of photocarriers.[62] Subsequently, electrons migrating to the surface of Ti_3C_2 MXene can further induce the formation of a range of ROS.[61] First, electrons reduce the dissolved oxygen (O_2) to $^{\bullet}O_2^-$ free radicals (eqn (4)),[61,62] while the $^{\bullet}O_2^-$ radicals may also react with H^+ and electrons to form H_2O_2 (eqn (5)).[61,63] In addition, H_2O_2 is dissociated by electrons to form $^{\bullet}OH$ radicals (eqn (6)).[61,63] At the same time, h^+ on the CdS valence band can directly oxidize water molecules or react with –OH to generate $^{\bullet}OH$ radicals (eqn (7)).[62,64,65] Generally, these reactive radicals with strong oxidizing properties can promote the degradation and transformation of organic contaminants (eqn (8)). In addition, the evaporation/catalytic system constructed by MC composite hydrogels has an inherent solid–liquid–gas triple-phase interface during operation,[66] where the water at the hydrogel-atmosphere interface is effectively evaporated under sunlight,[67] the organic contaminants migrate simultaneously to the surface of the hydrogels under the action of water transport and are fully in contact with the abundant reactive sites in the hydrogels. The water and oxygen molecules at the interface are combined with the charge carriers generated by the photoexcitation of the photocatalytic materials in the hydrogels and converted into $^{\bullet}O_2^-$ and $^{\bullet}OH$ free radicals,[66] and finally, a variety of ROS co-degrade organic pollutants. Ultimately, MC composite hydrogels with integrated photothermal and photocatalytic functions can produce safe water through solar-driven water evaporation and wastewater purification.

$$Ti_3C_2\ MXene/CdS + h\nu \rightarrow Ti_3C_2\ MXene\ (e^-) + CdS\ (h^+) \quad (3)$$

$$O_2 + Ti_3C_2\ MXene\ (e^-) \rightarrow {}^{\bullet}O_2^- \quad (4)$$

$$2H^+ + {}^{\bullet}O_2^- + e^- \rightarrow H_2O_2 \quad (5)$$

$$H_2O_2 + e^- \rightarrow {}^{\bullet}OH + OH^- \quad (6)$$

$$CdS\ (h^+) + H_2O/OH^- \rightarrow {}^{\bullet}OH \quad (7)$$

$$Contaminants + {}^{\bullet}O_2- + {}^{\bullet}OH + h^+ \rightarrow oxidation\ products \quad (8)$$

4 Conclusion

In summary, Ti_3C_2 MXene/CdS hydrogels (MCHs) with porous interconnect network structures were successfully prepared in this study. The hydrogels exhibit good hydrophilicity, light absorption, and photothermal effect, which induce excellent performance of solar-driven interfacial water evaporation and photocatalytic wastewater purification. The water evaporation rate of MCHs is 1.80 kg m^{-2} h^{-1} under one sunlight intensity. In addition, MCHs were able to efficiently remove various organic contaminants, such as antibiotics (metronidazole) and a typical VOC (phenol). From this work, it can be inferred that MCHs are the promising synergistic photothermal evaporation and photocatalytic materials, providing a potential pathway for sustainable clean water production in the solar-driven interfacial water evaporation technology field.

Author contributions

Zhen-Yu Wang: conceptualization, methodology, data curation, writing-original draft, investigation, formal analysis, visualization. Lei Xu: formal analysis, validation, methodology, data curation. Cai-Hua Liu: data curation, formal analysis, visualization. Sheng-Jie Han: validation and review. Ming-Lai Fu: supervision, resources, funding acquisition, writing-reviewing and editing. Baoling Yuan: funding acquisition, writing-reviewing and editing.

Conflicts of interest

There are no conflicts to declare.

Acknowledgements

This work was supported by the Major Program of the National Natural Science Foundation of China (52293444), National Natural Science Foundation of China (Grant No. 51978638 and 51778598), the Guiding Project of Fujian Science and Technology Plan (2023Y0025) and the Scientific Research Funds of Huaqiao University (20BS109, 21BS124).

References

1 Z. Mo, D. Li and Q. She, *Desalination*, 2022, **544**, 116147.
2 Y. Lv, S. Wu, J. Liao, Y. Qiu, J. Dong, C. Liu, H. Ruan and J. Shen, *Desalination*, 2022, **527**, 115537.
3 D. U. Lawal, M. A. Antar, K. G. Ismaila, A. Khalifa and S. M. Alawad, *Desalination*, 2023, **548**, 116231.
4 Y. Guo, X. Zhou, F. Zhao, J. Bae, B. Rosenberger and G. Yu, *ACS Nano*, 2019, **13**, 7913–7919.
5 Z. Gao, H. Yang, J. Li, L. Kang, L. Wang, J. Wu and S. Guo, *Appl. Catal., B*, 2020, **267**, 118695.
6 R. Chen, X. Wang, Q. Gan, T. Zhang, K. Zhu and M. Ye, *J. Mater. Chem. A*, 2019, **7**, 11177–11185.
7 P. Sun, W. Zhang, I. Zada, Y. Zhang, J. Gu, Q. Liu, H. Su, D. Pantelić, B. Jelenković and D. Zhang, *ACS Appl. Mater. Interfaces*, 2019, **12**, 2171–2179.
8 Y. Bu, Y. Zhou, W. Lei, L. Ren, J. Xiao, H. Yang, W. Xu and J. Li, *J. Mater. Chem. A*, 2022, **10**, 2856–2866.
9 J.-Y. Wang, X.-X. Guo, J. Chen, S.-C. Hou, H.-J. Li, A. Haleem, S.-Q. Chen and W.-D. He, *Mater. Adv.*, 2021, **2**, 3088–3098.
10 C. Chen, L. Zhou, J. Yu, Y. Wang, S. Nie, S. Zhu and J. Zhu, *Nano Energy*, 2018, **51**, 451–456.
11 H. D. Kiriarachchi, F. S. Awad, A. A. Hassan, J. A. Bobb, A. Lin and M. S. El-Shall, *Nanoscale*, 2018, **10**, 18531–18539.
12 P. Liu, X.-Y. Li, L. Xu, C. Chen, B. Yuan, L. Labiadh, Y.-b. Hu and M.-L. Fu, *Desalination*, 2022, **527**, 115532.
13 J.-L. Wu, S.-J. Han, L. Xu, Z.-Y. Wang, L. Labiadh, M.-L. Fu and B. Yuan, *Sep. Purif. Technol.*, 2023, **326**, 124759.
14 S. Yan, H. Song, Y. Li, J. Yang, X. Jia, S. Wang and X. Yang, *Appl. Catal., B*, 2022, **301**, 120820.

15 D. Qi, Y. Liu, Y. Liu, Z. Liu, Y. Luo, H. Xu, X. Zhou, J. Zhang, H. Yang, W. Wang and X. Chen, *Adv. Mater.*, 2020, **32**, 2004401.
16 P. Zhang, F. Zhao, W. Shi, H. Lu, X. Zhou, Y. Guo and G. Yu, *Adv. Mater.*, 2022, **34**, 2110548.
17 C. Song, D. Qi, Y. Han, Y. Xu, H. Xu, S. You, W. Wang, C. Wang, Y. Wei and J. Ma, *Environ. Sci. Technol.*, 2020, **54**, 9025–9033.
18 B. Chen, X. Zhang, Y. Xia, G. Liu, H. Sang, Y. Liu, J. Yuan, J. Liu, C. Ma, Y. Liang, M. Song and G. Jiang, *J. Mater. Chem. A*, 2021, **9**, 2414–2420.
19 J. Ma, L. An, D. Liu, J. Yao, D. Qi, H. Xu, C. Song, F. Cui, X. Chen, J. Ma and W. Wang, *Environ. Sci. Technol.*, 2022, **56**, 9797–9805.
20 X. Chen, Y. Guo, R. Bian, Y. Ji, X. Wang, X. Zhang, H. Cui and J. Tian, *J. Colloid Interface Sci.*, 2022, **613**, 644–651.
21 P. Liang, L. Yuan, K. Du, L. Wang, Z. Li, H. Deng, X. Wang, S.-Z. Luo and W. Shi, *Chem. Eng. J.*, 2021, **420**, 129831.
22 M. Alhabeb, K. Maleski, B. Anasori, P. Lelyukh, L. Clark, S. Sin and Y. Gogotsi, *Chem. Mater.*, 2017, **29**, 7633–7644.
23 A. VahidMohammadi, J. Rosen and Y. Gogotsi, *Science*, 2021, **372**, eabf1581.
24 S. Yu, H. Tang, D. Zhang, S. Wang, M. Qiu, G. Song, D. Fu, B. Hu and X. Wang, *Sci. Total Environ.*, 2022, **811**, 152280.
25 S. K. Sharma, A. Kumar, G. Sharma, D.-V. N. Vo, A. García-Peñas, O. Moradi and M. Sillanpää, *Chemosphere*, 2022, **291**, 132923.
26 D. Xu, Z. Li, L. Li and J. Wang, *Adv. Funct. Mater.*, 2020, **30**, 2000712.
27 Y. Wang, X. Wang, Y. Ji, R. Bian, J. Li, X. Zhang, J. Tian, Q. Yang and F. Shi, *Int. J. Hydrogen Energy*, 2022, **47**, 22045–22053.
28 B. Zhang, P. W. Wong and A. K. An, *Chem. Eng. J.*, 2022, **430**, 133054.
29 Z. Wu, X. Chen, B. Yuan and M.-L. Fu, *Chemosphere*, 2020, **239**, 124745.
30 P. Liu, Y. b. Hu, X. Y. Li, L. Xu, C. Chen, B. Yuan and M. L. Fu, *Angew. Chem., Int. Ed.*, 2022, **134**, e202208587.
31 P. Liu, L. Xu, Z. Y. Wang, Y. Huo, Y. b. Hu, M. L. Fu and B. Yuan, *ChemSusChem*, 2023, **16**, e202300611.
32 S.-J. Han, L. Xu, P. Liu, J.-L. Wu, L. Labiadh, M.-L. Fu and B. Yuan, *ChemSusChem*, 2023, **16**, e202300845.
33 R. Li, L. Zhang, L. Shi and P. Wang, *ACS Nano*, 2017, **11**, 3752–3759.
34 Z. Wang, W. Xu, K. Yu, S. Gong, H. Mao, R. Huang and Z. Zhu, *Sol. RRL*, 2021, **5**, 2100183.
35 W. Qu, H. Zhao, Q. Zhang, D. Xia, Z. Tang, Q. Chen, C. He and D. Shu, *ACS Sustain. Chem. Eng.*, 2021, **9**, 11372–11387.
36 B. Sun, P. Qiu, Z. Liang, Y. Xue, X. Zhang, L. Yang, H. Cui and J. Tian, *Chem. Eng. J.*, 2021, **406**, 127177.
37 R. T. Ginting, H. Abdullah, D. A. Barus and V. Fauzia, *J. Mater. Chem. A*, 2023, **11**, 5296–5308.
38 B. Zhang, Q. Gu, C. Wang, Q. Gao, J. Guo, P. W. Wong, C. T. Liu and A. K. An, *ACS Appl. Mater. Interfaces*, 2021, **13**, 3762–3770.
39 J.-Y. Li, Y.-H. Li, F. Zhang, Z.-R. Tang and Y.-J. Xu, *Appl. Catal., B*, 2020, **269**, 118783.
40 M. Ding, R. Xiao, C. Zhao, D. Bukhvalov, Z. Chen, H. Xu, H. Tang, J. Xu and X. Yang, *Sol. RRL*, 2020, **5**, 2000414.
41 C. Lei, J. Park, W. Guan, Y. Zhao, K. P. Johnston and G. Yu, *Adv. Funct. Mater.*, 2023, **33**, 2303883.
42 W. Li, X. Li, W. Chang, J. Wu, P. Liu, J. Wang, X. Yao and Z.-Z. Yu, *Nano Res.*, 2020, **13**, 3048–3056.
43 D. Fan, Y. Lu, H. Zhang, H. Xu, C. Lu, Y. Tang and X. Yang, *Appl. Catal., B*, 2021, **295**, 120285.
44 H. Wang, P. Hu, J. Zhou, M. B. J. Roeffaers, B. Weng, Y. Wang and H. Ji, *J. Mater. Chem. A*, 2021, **9**, 19984–19993.
45 X. Mu, L. Chen, N. Qu, J. Yu, X. Jiang, C. Xiao, X. Luo and Q. Hasi, *J. Colloid Interface Sci.*, 2023, **636**, 291–304.
46 L. Ding, S. Zeng, W. Zhang, C. Guo, X. Chen, B. Peng, Z. Lv, H. Zhou and Q. Xu, *ACS Appl. Energy Mater.*, 2022, **5**, 11540–11552.
47 X. Chen, Z. Wu, D. Lai, M. Zheng, L. Xu, J. Huo, Z. Chen, B. Yuan and M.-L. Fu, *J. Mater. Chem. A*, 2020, **8**, 22645–22656.
48 L. Song, L. Geng, Y.-p. Tian, P. Mu and J. Li, *J. Mater. Chem. A*, 2021, **9**, 23117–23126.
49 H. Zhang, L. Li, L. Geng, X. Tan, Y. Hu, P. Mu and J. Li, *Chemosphere*, 2023, **311**, 137163.
50 H. Bai, P. He, L. Hao, Z. Fan, R. Niu, T. Tang and J. Gong, *Chem. Eng. J.*, 2023, **456**, 140994.
51 Y. Lu, D. Fan, Y. Wang, H. Xu, C. Lu and X. Yang, *ACS Nano*, 2021, **15**, 10366–10376.
52 J. Zhang, J. Ma, D. Liu, D. Liu, Y. Han, Y. Xu, F. Cui and W. Wang, *J. Mater. Chem. A*, 2022, **10**, 10548–10556.
53 R. Long, Z. Yu, Q. Tan, X. Feng, X. Zhu, X. Li and P. Wang, *Appl. Surf. Sci.*, 2021, **570**, 151244.
54 Y. Lv, K. Wang, D. Li, P. Li, X. Chen and W. Han, *Chem. Phys.*, 2022, **560**, 111591.
55 H. Yu, H. Jiang, X. Cao and S. Yao, *RSC Adv.*, 2023, **13**, 16602–16609.
56 R. Chen, T. Zhang, J. Kim, H. Peng, M. Ye and C.-H. Huang, *Environ. Sci. Technol.*, 2021, **55**, 6248–6256.
57 N. An, R. Su, Z. Wang, W. Chen, W. Zhou and Q. Li, *Desalination*, 2023, **565**, 116849.
58 H. Mo and Y. Wang, *Water Res.*, 2022, **226**, 119276.
59 J. Deng, S. Xiao, B. Wang, Q. Li, G. Li, D. Zhang and H. Li, *ACS Appl. Mater. Interfaces*, 2020, **12**, 51537–51545.
60 R. Xiao, C. Zhao, Z. Zou, Z. Chen, L. Tian, H. Xu, H. Tang, Q. Liu, Z. Lin and X. Yang, *Appl. Catal., B*, 2020, **268**, 118382.
61 Z. Yang and J. Wang, *Langmuir*, 2023, **39**, 4179–4189.
62 Y. Bao, Y. Liu, Z. Zhang, J. Pan, X. Li, B. Zhao, R. Wang and J. Liu, *Chemosphere*, 2022, **307**, 136118.
63 X. Zou, X. Zhao, J. Zhang, W. Lv, L. Qiu and Z. Zhang, *J. Hazard. Mater.*, 2021, **413**, 125424.
64 J. Ren, L. Wang, Q. Gong, J. Xuan, M. Sun, Q. Zhang, H. Zhang, G. Yin and B. Liu, *New J. Chem.*, 2022, **46**, 3305–3314.
65 D. You, Z. Pan and Q. Cheng, *J. Alloys Compd.*, 2023, **930**, 167069.
66 Q. Xia, C. Wang, N. Xu, J. Yang, G. Gao and J. Ding, *Adv. Funct. Mater.*, 2023, **33**, 2214769.
67 Y. Pang, X. Chu, L. Song, L. Jin, C. Ma, Y. Wu, L. Li, Y. Peng, X. Zheng, F. Wang, S. Wu, Z. Shen and H. Chen, *Chem. Eng. J.*, 2024, **479**, 147891.